

For submission to: Journal of Chemical Physics

**Intramolecular vibrational relaxation in aromatic molecules II:
an experimental and computational study of pyrrole
and triazine near the IVR threshold**

A. Callegari^{1,†}, R. Pearman^{2†}, Susan Choi,^{1†} Peter Engels^{1†} H. Srivastava,^{1†}

M. Gruebele^{2,3}, K. K. Lehmann¹ and G. Scoles¹

Department of Chemistry,¹ Princeton University, Princeton, New Jersey 08544 and

*Departments of Chemistry,² Physics,³ Center for Biophysics and Computational Biology,²
University of Illinois, Urbana, IL 61801.*

Abstract

The threshold region of vibrational energy redistribution (IVR) presents a great experimental and computational challenge for organic molecules with more than 10 degrees of freedom. The density of states is sufficiently high to require very high resolution measurements to cover all relevant time scales experimentally. Yet it is sufficiently low so IVR quantities, such as the initial relaxation time τ_{IVR} or the number of participating states N_{eff} , are very sensitive to the coupling structure. To extend a previous study of benzene [A. Callegari et al., J. Chem. Phys. (2000)], we have measured overtone spectra of pyrrole (C_4H_4NH) and 1,2,3-triazine ($C_3N_3H_3$) by eigenstate-resolved double resonance spectroscopy, and performed large scale computations of IVR dynamics by using

analytically fitted fourth order *ab-initio* force fields and filter diagonalization. The modeled N_{eff} and τ_{IVR} agree with the experimental quantities within a factor of 2 to 3, reasonable for a rate theory in the threshold regime. The models also correctly predict the experimentally observed trends of τ_{IVR} and N_{eff} for the two molecules, and provide insight into the highly off-resonant coupling mechanism, which nonetheless yields very sharp linewidths. The series benzene-pyrrole-triazine highlights the competing effects of molecular symmetry on the accessible density of states and mode localization.

[†] Present addresses

AC: *École Polytechnique Fédérale, Lausanne, Switzerland.*

RP: *Columbia University, Dept. of Chemistry.*

PE:

1. Introduction

1.1 Background

During the past decade, traditional methods of analyzing IVR have been supplemented by new approaches such as quantum diffusion.^{1,2} In particular, a direct connection has been made between the full vibrational Hamiltonian and the IVR lineshape.³⁻⁶ Making this connection required several experimental and theoretical advances. On the experimental side, new high-resolution techniques have been able to resolve eigenstate structure in sizeable molecules, allowing statistical analyses of unprecedented quality;⁷⁻¹⁰ extensive high-overtone surveys¹¹ and isotopomer studies are possible;¹² both time- and energy-resolved experiments have revealed a transition to sub-exponential dephasing at long times;^{5,13,14} On the theoretical side, powerful new analysis techniques have made the most of survey spectra, extracting an enormous amount of detail about the underlying Hamiltonian;¹⁵ IVR, recognized as a highly structured process, is best described in terms of a local density of states which imposes structure on the quantum state space of polyatomic molecules (figure 1).^{14,16,17} Phenomena such as IVR thresholds, nonexponential decays and gateway states have been addressed in detail.¹⁸ A quantitative comparison between experimental initial lifetimes, dilution factors or IVR manifold dimensional exponents is now within reach.

These findings have significant implications for dissociation reactions. The seminal statistical work, RRKM theory, forms one of the successful bases of modern rate theories.¹⁹ The local character of IVR does not invalidate such rate models in the thermal near-threshold regime; IVR is sufficiently faster than thermal reaction time scales. Yet the existence of IVR thresholds^{20,21} and sub-exponential long-time dynamics has implications for the nonstatistical behavior of photochemical or other above-threshold reactive processes in organic molecules. There, reaction rates are sufficiently fast that the effects of IVR can be observed experimentally, and perhaps even controlled. Examples include anomalous isotope effects in stilbene isomerization,²² nonstatistical dissociation of the acetone enol radical cation,[Brauman] multiple-resonance induced isomerization of halobutyne,¹⁰ and the prediction that IVR can be 'frozen' beyond the reaction time scale.²

All this is a consequence of much remnant local structure in the molecular Hamiltonian at high vibrational energies: during dissociation, only six vibrational modes are converted into rotranslational motion, a number small compared to the total number of modes of a large organic molecule. The couplings among the remaining modes can be reduced to a local form. One can take advantage of this idea because an initially excited spectral feature will not have direct access to all of state space, only to a very small number of gateway states, which then communicate the excess vibrational energy to the remaining rovibrational manifold. These gateways can be plotted as on- or off-resonant in a ladder diagram,^{23,24} or the anisotropy of the energy flow can be fully visualized in a state space diagram (figure 1).^{17,25}

A particularly difficult - and therefore fruitful - region for comparison between modeling and experiments lies near the IVR threshold.^{7,26} Low resolution experiments, analyzed by local random matrix models and mean-field theories, have shown that the threshold region is sharply defined in terms of the local density of states, but not in terms of energy or total density of states:²⁷ when the local density of states significantly exceeds unity, a continuous network of coupled states can be established. The dilution factor

$$\sigma = \left(\frac{\sum_{g=1}^n I_g^2}{\sum_{j=1}^n I_j^2} \right)^2, \quad [1.1]$$

(inverse of the effective number of states N_{eff} participating in IVR, figure 1) and the initial decay rates fluctuate sharply in this regime. The reason for this is simple: gateway states are by definition very sparse near threshold, so couplings tend to be off-resonant and the precise disposition of gateway energies and coupling strengths is critical. In large molecules, this problem has been successfully dealt with by models which combine statistical elements with a scaled vibrational Hamiltonian. These models are quantitatively successful above the IVR threshold;¹⁴ at threshold, they can only predict averages and moments of IVR quantities for groups of similar molecules.²⁷

Here we present detailed experimental and theoretical results for the molecules pyrrole (24 vibrational degrees of freedom,) and triazine (21 vibrational degrees of freedom) near the IVR threshold, as a continuation of a previous study of benzene.⁹ The $2\nu_{14}$ CH stretching overtone was chosen for pyrrole, and the combination band $\nu_6 + 2\nu_7^2$ for triazine. For these states $\sigma > 0.01$, but

there is still a substantial number of participating states. The initial decay lifetimes exceed several picoseconds because the IVR threshold has just been reached. These bands lie at roughly the same energy as the $2v_{14}$ band previously studied for benzene. The availability of fully resolved experimental eigenstate spectra near threshold presents a challenge for computational models. We use spectroscopically fitted *ab-initio* coordinate potentials and eigenstate calculations in the full 21- to 24-dimensional vibrational state spaces to meet this challenge. The off-resonant nature of most interactions near threshold makes this particularly difficult; reasonable agreement with experimental dilution factors and initial decay rates is obtained if a uniform underestimate of bright-dark couplings by the Hartree-Fock *ab-initio* surface is taken into account. The calculations allow a discussion covering all energy scales, from low resolution 'satellites' down to the eigenstates.

1.2 Previous work on pyrrole, triazine and benzene

The structure and vibrational spectrum of pyrrole have been investigated several times since the first reported data and vibrational analysis of Lord and Miller²⁸ experimentally by microwave²⁹ and Infrared/Raman^{30,31} spectroscopy, as well as theoretically with *ab initio*³² and algebraic methods³³. The CH stretch fundamentals have been investigated in the past at low resolution by various authors with some contradictory assignments. [References]

More recently, Held and Herman³¹ have resolved the ambiguity with a high-resolution investigation of the fundamental CH region. Lubich and Oss³³ have addressed the overtone problem starting from a semi-empirical one-dimensional algebraic model based on which, they predict the position and intensity of all the overtones and combination bands of the CH and NH stretches in the 6000-7000 cm⁻¹ region. To the best of our knowledge the full dynamics of the overtone region has never been investigated before.

1,3,5-Triazine (C₃H₃, henceforth referred to simply as triazine) is the most symmetric of the three possible isomers and the most stable one. The molecular structure and vibrational modes of triazine and some of its derivatives have been determined experimentally by infrared/raman spectroscopy³⁴⁻³⁸, electron^{34,38} and neutron³⁹ scattering and theoretically by *ab initio* calculations

^{34,36,38-40}. Triazine dynamics has been the subject of a number of investigations, mostly in the excited electronic surface. Only recently the controversy about the photodissociation mechanism (two step vs. concerted triple dissociation) has been resolved⁴¹ in favor of the two step mechanism. Very little is known about the dynamics of the molecule in the ground electronic state potential energy surface (see ref. ³⁴ and references therein).

Pyrrole and triazine having been chosen for comparison with a previous investigation of IVR dynamics of benzene in the same energy region. Therefore it is important to point out the relevant differences between the three molecules. Strictly speaking, the absence of a high order symmetry axis makes pyrrole an asymmetric top, with all the 24 normal modes of vibration infrared allowed. Most of the asymmetry is caused by the small carbon-nitrogen mass difference, so pyrrole is nearly an oblate symmetric top (≈ 0.9438). From the point of view of dynamics, the reduced symmetry compared to benzene implies that the vibrational states are distributed among fewer symmetry classes, so there is a higher probability that two states belong to the same class and therefore can be mixed by anharmonic terms in the Hamiltonian. The increase in the available density of states due to the lower symmetry is offset by the decrease of the total density of states due to the smaller number of atoms, and the expected active density of vibrational states is calculated to be 30 % below that of benzene. This does not include the role played by rotational degeneracy. Absent vibration-rotation interaction, the projection K of the angular momentum on the high symmetry molecular axis is a strictly conserved quantum number in symmetric top molecules. In a near symmetric top, the full $2J+1$ K states become available, but only at high J . Finally, pyrrole has more classes of inequivalent bonds than benzene, which could give rise to more localized vibrations and weaker effective couplings. Triazine is an intermediate case: like benzene, delocalized normal modes arise from the high molecular symmetry (D_{3h}); like pyrrole, there are inequivalent atoms in the ring.

2. Experiment and analysis

2.1 Experimental Approach

The experimental apparatus has been described in detail before[References] and a review of it is given in the previous paper of this series,⁹ so only a brief summary will be given here, along with the few changes implemented specifically for this experiment. A cold molecular beam is formed by co-expanding a 0.5-1% mixture of pyrrole or triazine in helium through a 50 μm nozzle. Upon collimation by a 0.5 mm skimmer, the beam enters a second vacuum chamber where it is probed by an infrared 1.5 μm laser and detected further downstream by means of a cryogenically cooled silicon bolometer. Laser excitation occurs inside a resonant power build-up cavity placed across the beam, which enhances the effective laser power experienced by the molecules by a factor of about 500.

Instead of making a pre-mixed sample of pyrrole in helium, the mixture was formed directly at the gas inlet of the spectrometer by bubbling pure helium at about 400 kPa through a stainless steel cylinder containing liquid pyrrole (Acros, > 99% purity). This has the advantage that the dilution of the mixture can be easily changed by changing the temperature of the cylinder, allowing suppression of dimers. Dimer formation was further prevented by keeping the nozzle and the gas inlet line heated to about 70 °C.

A beam of triazine was made by flowing 400 kPa helium gas through a stainless steel cilinder containing a few grams of solid triazine (Aldrich 97% purity, used without further purification). Air was eliminated from the container by repeated cycles of pumping and flushing with helium. The container was refilled every four hours with fresh triazine in order to keep the beam composition reasonably constant. Both the container and the gas line connecting it to the nozzle were kept at a temperature of about 75 °C to increase the concentration of triazine in the beam. The nozzle was kept at a higher temperature (~ 90 °C) to avoid condensation of triazine in the nozzle. This yielded a 0.5 % mixture.

We have added to the spectrometer the capability of doing microwave-infrared double resonance for the purpose of labeling the different rotational states of pyrrole. Microwave radiation from a Hewlett Packard 8350B frequency sweep oscillator was coupled into the spectrometer

through a mica window and brought to the interaction region by a 30 cm long strand of (K band) flexible waveguide. The microwave frequency was monitored with a frequency counter with a precision of $1/10^8$. Because the available power (100 mW) saturates the strong rotational transitions of pyrrole, we made no attempt to optimize coupling efficiency. A 2 mm gap in the waveguide allowed for the allowed the microwaves to be modulated by a chopper blade. During single resonance, the IR beam was chopped at 280 Hz instead. The bolometer signal was detected with a lock-in amplifier (Stanford Research 510). In the case of single resonance spectra, all transitions are detected and appear in the spectrum as positive peaks whose height is proportional to the population of the lower state and the fraction of bright state character carried by the upper state. In the case of a double resonance experiments, only those infrared transitions whose ground state population is affected by the microwave are detected. They appear either as positive or negative peaks, depending on whether the shared state is the upper or lower state of the microwave transition. The double resonance signal was generally lower because of the smaller population difference, but sufficient to allow firm assignments.

2.2 Ro-vibrational analysis

Figures 2 and 3 show the observed molecular beam spectra of pyrrole and triazine, along with simulations using the parameters in table 2.1. In both cases comparison between the experimental and simulated spectrum reveals that the fractionation of spectral lines induced by vibrational coupling is extensive but not sufficient to obscure the rotational band-structure. This already puts a visual upper limit to the IVR rate since the width of each multiplet must be smaller than or comparable with the spacing between rotational clumps.

In the case of pyrrole, the band has been assigned by Lubich and Oss ³³ to the *a*-type 2_{14} overtone. The rotational structure typical of the perpendicular band of a planar quasi-symmetric top—clusters of lines separated by a distance $2(A-B)$ —is clearly recognizable. Spectral assignment was carried out by combination differences involving transitions to the same J_{KaKc} state, making use of the fact that only the upper vibrational state is fragmented by IVR. The ground state rotational constants are known with sufficient accuracy to assign the spectrum by looking for identical

patterns of lines (corresponding to transitions to the same final state) separated by the same energy difference as the ground rotational levels. Assignments were further confirmed by microwave-infrared double resonance, as shown in figure 4.

We focus on the progression $J_{0,J} - J_{0,J\pm 1}$ as it is the strongest and most completely assigned. Figure 5 shows a comparison between various IVR multiplets belonging to this progression. Note that for small J , the splitting pattern remains roughly the same, an indication that anharmonic couplings dominate over Coriolis couplings in determining the IVR dynamics. At high J , the line density increases by more than a factor of two, and the width of the feature decreases from 0.25 to 0.15 cm^{-1} , giving a time-scale for IVR dynamics of several tens of picoseconds.

In the case of triazine, the exact identity of the observed band is less definitive. Five bands are expected to carry significant infrared intensity in the first CH stretching overtone region. They all have the E' symmetry required for mixing with the in-plane CH stretches which carry transition moment in this spectral region. The five bands derive from various combinations of the E' symmetry Fermi dyad $|_6\rangle$ (CH stretching) $|2_7\rangle^2$ (ring breathing mode overtone) with the A' symmetry levels $|_1\rangle$ (symm. CH stretching) and $|2_7\rangle^0$, namely: $|_1+|_6\rangle$, $|2_6\rangle^2$, $|_1+2_7\rangle^2$, $|_6+2_7\rangle^0$ and $|-6+2_7\rangle^2$. A low resolution FTIR spectrum of the overtone region (figure 6) shows the most intense band centered approximately at 5980 cm^{-1} , which was chosen for our investigation. Based on its frequency and its Coriolis constant (λ obtained from the molecular beam spectrum), the band has been assigned as carrying mostly $|_6+2_7\rangle^2$ combination character, with admixture from the remaining four states.

Triazine does not have a permanent dipole moment, hence microwave double-resonance techniques cannot be used to assign the spectrum. Assignment was carried out by combination differences only, using the ground states rotational constants of ref.³⁷ Numerical simulation of the spectrum was based on the symmetric top hamiltonian⁴²:

$$= |_0\rangle + (B'+B'') m + (B'-B''-D'+D'') m^2 - 2(D'+D'') m^3 - (D'-D'') m^4 + [C'(I-2\zeta) - B'] + 2[C'(I-\zeta)-B'] k + [(C'-B')-(C''-B'')]k^2, \quad [2.1]$$

where $m=J''+1$ for the R branch and $m= -J''$ for the P branch, $k= K''$ for $K= +1$ transitions and $k= -K''$ for $K= -1$ transitions. As a first approximation, the upper state rotational constants were set equal to the ground state value and then refined as the assignment progressed (table 2.1). Of the about 3000 transitions observed in the experimental spectrum, approximately 300 among the most intense have been assigned by combination differences their J and K quantum numbers. The low J , K multiplets are rather complete, so an analysis of the IVR dynamics and its dependence on molecular rotations can be carried out.

2.3 Experimental IVR analysis

For problems involving very large numbers of coupled states, it is not possible to fully characterize the resulting eigenstates. Nor are state-of-the-art computational methods sufficiently accurate to allow for a meaningful comparison of experiment and theory at the individual eigenstate level. We are therefore interested in ensemble properties derived from experiment, like the IVR lifetime (τ_{IVR}), the distribution of intensities and eigenstate spacings, and the number of participating states N_{eff} . Although the connection between the spectrum and most of these properties is straightforward, a short explanation is in order. The experimental density of coupled states (ρ_{exp}) is computed as the ratio between the number of observed state and the energy interval they occupy: $\rho_{exp} = (N-I)/\Delta E$. The average coupling (V_{rms}) between bright state and the bath is computed by Lawrence-Knight deconvolution with the improved algorithm of Ref. ⁴³. The IVR lifetime (τ_{IVR}) and its inverse, the IVR rate (k_{IVR}), are then computed from the Golden Rule:

$$k_{IVR} = \frac{2\pi V_{rms}^2 \rho}{\hbar} \quad [2.2]$$

The dilution factor ρ and the related effective number of participating states ($N_{eff} = \rho^{-1}$), are computed from the normalized spectral intensities according to eq. 1.1. Additional details of this analysis and further references can be found in the previous paper of this series.⁹ Tables [2.2] through [2.4] summarize the experimental results for pyrrole and triazine.

In the case of pyrrole, the measured density of coupled states ρ_{exp} ranges from $92/\text{cm}^{-1}$ to $251/\text{cm}^{-1}$ for the 2_{02} and 7_{07} multiplets respectively, and exhibits an almost monotonic increase with

J. The total density of vibrational states available for coupling can be reasonably well estimated from the fundamental frequencies [refs] by using the Laplace transform method described in.⁴⁴ The estimated value $\nu_{\text{calc}} = 93/\text{cm}^{-1}$ compares well with the experimental value of $92/\text{cm}^{-1}$ for $J=2$, indicating that a substantial fraction of the states available for coupling is actually observed. The increase of ν_{exp} with J is most likely the consequence of Coriolis coupling, but in the simple case where the dominant effect arises from Coriolis coupling between bright state and bath states, one would expect that V_{rms} in table [2.2] also increase with J , which is not the case. The real picture is more complicated, and Coriolis coupling affects more the coupling among bath states themselves, than the coupling between bright and dark states Correspondingly, the observed IVR lifetimes start from 60 ps for the low- J states 2_{02} and 2_{21} , generally increasing with J to about 100-110 ps at the high- J end. Given the gradual change, it seems reasonable to take the low- J value of 60 ps as an estimate of the IVR lifetime of the rotationless molecule.

We are not only interested in the rate of the IVR process but also in its mechanism. Although we cannot pinpoint the exact role of each bath state, we can quantify the extent to which the ensemble of all available bath states participate in the process. We focus on the low- J states dominated by anharmonic coupling because they are also computationally accessible. As seen above, most of the available states participate in the energy redistribution process. Furthermore, the effective number of coupled states (table [2.2]) is a substantial fraction of the total number of coupled states: essentially all symmetry-allowed participate to some extent in the IVR. On the other hand, the low- J multiplets reveal sub-structure in the form of clumps of spectral lines. This indicates preferential coupling between the bright state and certain bath 'gateway' states. This means that vibrational states are not randomly mixed with one another, and energy is not redistributed randomly to all of the states available in a given energy range (figure 1). To test the extent of vibrational mixing, we analyzed the level spacing distribution of each rotational multiplet. The probability of finding two eigenstates at a distance s is given by the empirical formula:⁴⁵

$$P(s) = as^\beta \exp(-bs^{\beta+1}) \quad a = (\beta + 1)b, \quad b = \frac{\beta + 2}{\beta + 1} \quad [2.3]$$

with β ranging from 0 for a system with uncorrelated energy levels to 1 for a system with randomly and strongly coupled energy levels. When performing this kind of analysis, we have to account for

the apparent spacing distribution differing from the real one because of the finite signal-to-noise ratio of the experiment. To this effect, we have calculated the actual density of states and, correspondingly, the fraction of them that would have to go undetected in order to give the same distribution of spacings that we observe, starting from a fully mixed ($\tau = 1$) system. The larger the discrepancy between the required density of states and a reasonable estimate for it, the less the energy redistribution can be described as random and complete.⁹ It is apparent from table [2.3] that low J pyrrole is not well described by a completely mixed system, unless one were to assume an unreasonably large density of vibrational states (cf. calculation of $93/\text{cm}^{-1}$). The situation is less clear at higher J , where the density of states corresponding to a complete IVR remains high, but within the boundaries of a reasonable estimate, if one allows the full $2J+1$ -fold increase arising from breakdown of the K symmetry. It is clear again that pyrrole IVR dynamics exhibits two different regimes. Extensive but nonrandom IVR at low J , where anharmonic coupling dominates; possibly complete IVR at higher J , where Coriolis coupling makes a significant contribution.

Analysis of the triazine spectrum (table 2.4) mainly differs from pyrrole in that only $N_{\text{eff}} = 4$ to 6 states are coupled. The observed density of states ranges in an interval similar to the one observed for pyrrole and is in reasonable agreement with the value of $63/\text{cm}^{-1}$ calculated from the harmonic frequencies via Laplace transform.⁴⁴ When a small number of coupled states is observed, large statistical fluctuations are possible.

We consider mainly the $J=0, K=0$ state, which classically corresponds to a non-rotating molecule, and is simulated in the next section. Selection rules forbid Coriolis coupling to this state, so any observed splitting must come from anharmonic coupling. Only one transition to this state is allowed (${}^3\text{P}_1(1)$), so there is no possibility of using combination differences for the assignment. Fortunately, as shown in figure 7, ${}^3\text{P}_1(1)$ is sufficiently isolated in the spectrum. The only overlapping lines belong to the ${}^3\text{Q}_3$ branch which has been reliably assigned, so the remaining lines observed in this portion of the spectrum can be safely assigned to ${}^3\text{P}_1(1)$. Because of the "rotationless" nature of this state, the value of its lifetime is particularly interesting. It gives the rate of IVR as mediated only by vibrational couplings. A value of $\tau_{\text{IVR}} = 115 \text{ ps}$ is computed from eq. [2.2]. Comparison with the other J states with $K=0$ shows a rather constant value of the lifetime at

low J with fluctuations at $J=3,4$ but no significant trend that would point to an onset of Coriolis coupling. The small number of coupled states does not allow the same kind of statistical analysis carried as for pyrrole.

3. IVR computations

3.1 Potential energy surfaces

Eigenstate resolved IVR calculations have been carried out at a high level of accuracy for several 6-dimensional systems using an *ab-initio* based vibrational Hamiltonian.^{5,6,46} Semi-empirical force fields have been used for larger substituted acetylenes.^{3,24} Full-dimensional quantum dynamics calculations using a scaled Hamiltonian⁴⁷⁻⁵¹ have appeared for systems ranging from propyne to fluorene.^{14,48,52} Recently, dynamics on a high-quality *ab-initio* based surface were computed up to 8 ps for all degrees of freedom of benzene.⁴ Here, we supplement the experimental results with full-dimensional vibrational spectrum calculations based on a spectroscopically fitted *ab-initio* Hamiltonian.

At excitation energies below 7,000 cm⁻¹, analytical potential surfaces can be constructed from a set of *ab initio* data points in the framework of a normal coordinate Hamiltonian.⁵ The experimentally observed densities of states near 100/cm⁻¹ make it unreasonable to expect line-by-line agreement between experiment and theory. Instead, we are interested in predicting overall spectral patterns, approximate band origins, gateway states that may appear in the spectra, dilution factors, and initial IVR decay times.

A normal coordinate potential surface was constructed for each molecule as follows: 1. A large number of molecular geometries was sampled by ab initio calculations. 2. A curvilinear coordinate set was chosen, and mapped into anharmonic curvilinear displacement coordinates. 3. A bilinear potential in these anharmonic coordinates was constructed to introduce anharmonic cross terms. 4. A fourth order normal mode potential energy surface was generated from the anharmonic curvilinear coordinate surface. Here, we discuss the procedure for triazine in detail; pyrrole was

treated analogously unless otherwise noted. Potential parameters for both molecules are fully described in ref.⁵³.

The electronic wavefunction was treated at the Hartree-Fock 6-31G** level, providing a reasonable tradeoff between accuracy and speed. First, a set of 1000 points up to 15,000 cm⁻¹ was selected to map out the potential energy surface, by applying random displacements away from the optimized equilibrium geometry in table 3.1. Higher energies were rejected from consideration because preliminary scaling considerations indicated that even in a normal mode state space,⁴⁹ the potential surface above 15,000 cm⁻¹ would not make significant contributions to the dilution factor. (It could still affect off-resonant shifts of band-origin.) After a preliminary constrained normal mode analysis, 10,000 more *ab-initio* data points were sampled using random linear combinations of normal mode displacements.

Next, we constructed an analytical internal coordinate representation { s_i }, from valence coordinates:

$$\text{Stretch: } r_{ij} \quad [3.1a]$$

$$\text{Bend: } \alpha_{ijk} \text{ (ring)} \text{ or } \beta_{ijk} \text{ (hydrogen)} \quad [3.1b]$$

$$\text{Wag: } \gamma_{ijkl} = \frac{(\vec{r}_{ij} \times \vec{r}_{ik}) \cdot \vec{r}_{il}}{|\vec{r}_{ij}| |\vec{r}_{ik}| |\vec{r}_{il}|} \quad [3.1c]$$

$$\text{Torsion: } \tau_{ijkl} = \cos^{-1} \frac{(\vec{r}_{ij} \times \vec{r}_{ik}) \cdot (\vec{r}_{ki} \times \vec{r}_{kl})}{|\vec{r}_{ij}| |\vec{r}_{ik}|^2 |\vec{r}_{kl}| \sin(\theta_{ijk}) \sin(\theta_{jkl})} . \quad [3.1d]$$

In these equations, i,j,k and l label atoms as shown in figure 8, which also gives examples of the valence coordinates as defined above. There is some redundancy in the valence coordinates used to construct the s_i . Group theory for the k ring atoms indicates the use k stretching coordinates, k-3 bending coordinates, and k-3 torsional coordinates to remove the redundancy. One can either construct symmetry-adapted coordinates s_i , or simply let the s_i be a subset of valence coordinates covering the right symmetries. For triazine, a truncated set of internal coordinates was used. The definition of the s_i is given in table 3.2. Finally, equilibrium values from table 3.1 were subtracted from the s_i as appropriate to create displacement coordinates x_i , also defined in table 3.2.

To allow adjustment of the anharmonicity, the curvilinear internal displacement coordinates x_i are transformed to f -potential coordinates:

$$f_i = f(x_i) = d_i \cdot 1 + \frac{(b_i - 1)\beta_i x_i}{m_i}^{-m_i} - 1 + \frac{b_i \beta_i x_i}{n_i}^{-m_i}. \quad [3.2]$$

These are described in detail elsewhere;^{49,54} briefly, β controls the degree of anharmonicity, b the symmetry of the potential well ($b = 1/2$ symmetric, $b = 1$ dissociative in one branch), and m the shape of the potential well (e.g. $m = -2$ is a Morse oscillator, $m = 6$ a Lennard-Jones potential, and $m = -2$ a harmonic oscillator). This representation ensures that the proper diagonal anharmonicity for the bright states (CH stretches) can be included.

Next, the ab initio data points were fitted to a curvilinear potential surface of the form⁵⁵

$$V_{\text{internal}} = \sum_{i=1}^{3N-6} F_{ij} f_i f_j. \quad [3.3]$$

Because the coordinates f are highly nonlinear functions of the valence coordinates, this second order expansion already contains high order diagonal and cross anharmonicities. The F_{ij} and the parameters in eq. [3.2] were fitted to the 11,000 *ab-initio* points. There are far fewer F_{ij} than the general case in eq. [3.3] because of symmetry, leading to the following specific form of the triazine potential surface:

$$\begin{aligned} V = & \sum_{i=1}^{21} f_i^2 + \sum_{k=1}^3 F_{CN\alpha}^{(k)} \sum_{i,j \in S_k} f_i^{CN} f_j^{CN} + \sum_{k=1}^3 F_{CN\beta}^{(k)} \sum_{i,j \in S_k} f_i^{CN} f_j^{\beta} + \sum_{k=1}^3 F_{CN\gamma}^{(k)} \sum_{i,j \in S_k} f_i^{CN} f_j^{\gamma} + \sum_{k=1}^3 F_{CN\tau}^{(k)} \sum_{i,j \in S_k} f_i^{CN} f_j^{\tau} + \\ & + \sum_{k=1}^3 F_{CH\alpha}^{(k)} \sum_{i,j \in S_k} f_i^{CH} f_j^{\alpha} + \sum_{k=1}^3 F_{CH\beta}^{(k)} \sum_{i,j \in S_k} f_i^{CH} f_j^{\beta} + \sum_{k=1}^3 F_{CH\gamma}^{(k)} \sum_{i,j \in S_k} f_i^{CH} f_j^{\gamma} + \sum_{k=1}^3 F_{CH\tau}^{(k)} \sum_{i,j \in S_k} f_i^{CH} f_j^{\tau} + \\ & + F_{\alpha\alpha}^{(1)} \sum_{i,j} f_i^{\alpha} f_j^{\alpha} + F_{\alpha\beta}^{(k)} \sum_{i,j \in S_k} f_i^{\alpha} f_j^{\beta} + F_{\alpha\gamma}^{(k)} \sum_{i,j \in S_k} f_i^{\alpha} f_j^{\gamma} + F_{\alpha\tau}^{(k)} \sum_{i,j \in S_k} f_i^{\alpha} f_j^{\tau} + F_{\beta\beta}^{(1)} \sum_{i,j} f_i^{\beta} f_j^{\beta} + \\ & + F_{\beta\gamma}^{(k)} \sum_{i,j \in S_k} f_i^{\beta} f_j^{\gamma} + F_{\beta\tau}^{(k)} \sum_{i,j \in S_k} f_i^{\beta} f_j^{\tau} + F_{\gamma\gamma}^{(1)} \sum_{i,j} f_i^{\gamma} f_j^{\gamma} + F_{\gamma\tau}^{(k)} \sum_{i,j \in S_k} f_i^{\gamma} f_j^{\tau} + F_{\tau\tau}^{(1)} \sum_{i,j} f_i^{\tau} f_j^{\tau} \end{aligned} \quad [3.4]$$

In this notation, the set S_k refers to all symmetry-equivalent coordinate combinations for any product $f_i f_j$. The summation over k refers to nearest neighbors ($k=1$), next-nearest neighbors ($k=2$) etc. The superscripts refer to r_{CN} (CN), the θ_{NCN} angle (), etc. Consider the two summations in the second term as an example. The first sums over three kinds of CN bond-bond couplings, nearest neighbors ($k=1$), next-nearest ($k=2$), and next-next nearest ($k=3$); as expected, the coupling constants $F_{CN\bar{C}N}^{(k)}$ decrease rapidly with bond separation. The second summation over three sets S_k takes into account all the possible pairs for each k . For $k=1$, these are $f_1 f_2, f_2 f_3 \dots, f_6 f_1$.

To increase fitting robustness further, the equilibrium geometry was held fixed at the values in table 3.1, and several d_i were constrained by known dissociation energies $D_{ii} = d_i^2$ ($F_{ii} = 1$). The fit was energy-weighted in order to increase its accuracy near the bottom of the well. The resulting fit had an error of $< 3\%$ for triazine, sufficient to reproduce the overall features of the potential surface at the same level of accuracy as the HF calculations themselves. Tables 3.2 and 3.3 show the best-fit parameters and potential constants F_{ij} for triazine.

Normal mode potential constants up to fourth order were numerically generated using a multi-point finite difference differentiation algorithm. The potential energy second derivative matrix was constructed first. The resulting normal mode displacements were used to compute third and fourth order directional derivatives.⁵ Convergence was checked as a function of stepsize and numerical precision, and found to be better than 1% for all potential constants. In particular, symmetry-forbidden potential constants were evaluated and found to be negligibly small. Finally, a scaling factor $\alpha_i^{n_i}$ was applied to potential constants of order n_i in mode i , to correct for the vibrational frequency overestimate inherent at the HF level of theory. The scaling was chosen to bring the harmonic vibrational frequencies into agreement with values estimated from experiment (Table 3.4 and 3.5). The adjustments ranged between $\alpha_i = \sqrt{\omega_{exp}/\omega_{calc}}$ α 0.90-1.00.

3.2 Spectral calculation

IVR spectra can be calculated from the potential surface by diagonalizing the Hamiltonian matrix. We now describe how this was done for the very large matrices required for the pyrrole and triazine IVR spectra.

Matrix elements were constructed for a Watson Hamiltonian second order in kinetic energy and fourth order in potential energy for $J=0$. Coriolis and vibrational angular momentum terms were neglected. In pyrrole, the latter are negligible at the energy in question. In triazine, they can lead to energy shifts of several cm^{-1} because of degeneracies, but do not contribute significantly to the off-resonant mixing important for IVR, and were also neglected. Because of the neglect of Coriolis couplings, the calculations should be compared to low J experimental data only. In order to obtain a good zero-order representation of the bright states, a mixed anharmonic-harmonic basis was used to construct the Hamiltonian matrix. One-dimensional cuts through the hydrogenic stretches were pre-diagonalized to yield optimized anharmonic basis functions; the remaining modes were treated in a harmonic basis. An alternative approach would be to use DVR functions, but we found the mixed anharmonic-harmonic basis suitable for the present purpose. No higher order corrections to the cubic and quartic matrix elements were included.

To generate a sparse matrix, matrix elements were chosen based on a tier algorithm. The bright state is the 'zeroth tier.' Further states are selected to be in the n^{th} tier if they have a coupling to the $(n-1)^{\text{th}}$ tier above a certain threshold. The threshold function is a measure of how much a state is coupled to another state:

$$\mathcal{L}_{ij} = \frac{1}{\sqrt{\left(1 + \frac{E_{ij}}{V_{ij}}\right)^2}} . \quad [3.5]$$

It has been shown elsewhere that for a given state i , ${}_j\mathcal{L}_{ij}^2$ is an effective measure of the local density of directly coupled states.^{27,50} States were accepted into a tier if their threshold parameter exceeded 0.003 (a very conservative value) to any state in the previous tier. Only states in a window $\pm \Delta E_{\text{max}} = \pm 4,000 \text{ cm}^{-1}$ were included in the calculation. This allows most, but not all (see section 4) off-resonant contributions to be taken into account. Levels which are not included up to final tier n are pruned out of the matrix, substantially reducing the size of the matrix. In practice, low

resolution searches for gateway states were carried out with 1-2 tiers after the bright state, and 'production' runs were carried out with three to four tiers. The basis set for pyrrole contains about 1/5 the actual density of states near the state of interest, or about 15-20 A₁ states/cm⁻¹. Similar calculations were carried out for triazine, but one larger calculation for triazine with 40-45 states/cm⁻¹ in the interval of interest (about half the expected density) was also carried out. A comparison between the smaller and more complete bases will be interesting and is presented in section 4 along with a comparison to experimental results. None of these basis sets can quite 'fill in the spectrum' as much as experiment; this would have required five to six tiers after the bright state, which is currently prohibitively expensive.

Even after tier-based pruning, the resulting matrices are still large (about 80,000 to 270,000 states), albeit very sparse due to the local coupling nature of the Hamiltonian.⁵⁶ Because of their large size, highly efficient diagonalization algorithms are required. In previous papers, we made use of the MFD-Lanczos algorithm, which requires no eigenvector calculations to extract the intensities of the spectrum in the full window.⁵⁷ The present IVR linewidths based on the experimental data are very narrow, less than 1 cm⁻¹. Therefore only a small energy window $\Delta E_{\text{feature}}$ out of the total $\pm \Delta E_{\text{max}}$ is needed. Two methods are therefore of potential interest: Preconditioned Lanczos diagonalization emphasizes eigenvalues near the energy of interest.⁵⁸ The second method, filter-diagonalization, automatically generate eigenvalues in a specified window.[Neuhauser]

We decided to test filter-diagonalization because it was the only relevant numerical method with which we had not acquired previous experience. Recently, a particularly useful version of such algorithms was developed by Mandelshtam and Taylor.⁵⁹ The crux of the Mandelshtam-Taylor algorithm is that it generates two small, non-symmetric Hamiltonian and overlap matrices H_{feature} and S_{feature} leading to a generalized eigenvalue problem which covers only the energy window of interest. This is achieved through Chebyshev propagation of an initial state $|\xi_0\rangle$ and generation of overlap coefficients $c_n = \langle \xi_0 | \xi_n \rangle$, using basis energies φ_j selected uniformly in the energy subinterval $\Delta E_{\text{feature}}$ containing the IVR feature of interest. Although one now solves a generalized eigenvalue problem, the size of the matrix is reduced by the ratio $E_{\text{feature}} / E_{\text{max}} = 1/1000$.

The intensities of the eigenstate peaks within the IVR feature can be extracted as well, and directly yield the desired spectrum if the state $|\xi_0\rangle$ corresponds to the bright state:

$$I_k = \sum_{j=0}^n B_{jk} \sum_{i=0}^M (2 - \delta_{i0}) \cos(i\phi_j) c_i^2. \quad [3.6]$$

Here n is the total number of energy points ϕ_j , and M the total number of Chebyshev iterations which generate the smaller matrices of size M . Because the rank of the eigenvalue problem can be less than n , the first summation is only over linearly independent basis points.

A few eigenvectors can also be extracted from this method by backpropagation, without requiring a significant memory or storage overhead. A useful property of the filter diagonalization process is that it converges on the eigenvectors with the largest intensity first and generally finds all states with an intensity greater than 0.1% of the maximum. However, the accuracy of eigenvalues is lower than that obtained by Lanczos methods with comparable effort: at best 0.001 cm^{-1} for the most intense levels, and $> 0.1 \text{ cm}^{-1}$ for states not well overlapped with $|\xi_0\rangle$. We expect preconditioned Lanczos iteration to provide better performance when highly accurate eigenvalues are required, such as in application of the MFD algorithm.⁶⁰

The choice of bright state $|\xi_0\rangle$ is trivial for pyrrole: we used the A_1 symmetry anharmonic $2v_{14}$ wave function. The choice is more complicated for the $v_6^1 + 2v_7^2$ band of triazine because of E symmetry in the bright state modes, as indicated by the ℓ quantum number superscripts. Our basis set is cartesian, so the conversions

Singly excited: $\Psi^1 = \Psi_A + i\Psi_B$

$$\Psi^{-1} = \Psi_A - i\Psi_B \quad [3.7a]$$

Doubly excited: $\Psi^0 = \Psi_{AA} + \Psi_{BB}$

$$\Psi^2 = \Psi_{AA} - \Psi_{BB} + i\Psi_{AB} \quad [3.7b]$$

$$\Psi^{-2} = \Psi_{AA} - \Psi_{BB} - i\Psi_{AB}$$

were applied. Because ℓ has little effect on the IVR in the rotationless case, real linear combinations preserving $|\ell\rangle$ were chosen to construct the initial state, to avoid the fourfold increase in matrix-diagonalization time required by complex initial vectors. We chose $v_6^1 + 2v_7^2 = \frac{1}{\sqrt{2}}(v_{6A} - v_{7AA})$ as the appropriate linear combination.

To evaluate the dependence of bright state fragmentation on the coupling strength to non-hydrogenic bath states, calculations were carried out with a scaling factor δ . δ was chosen as a uniform scaling factor for all matrix elements not involving exclusively changes in the hydrogenic quantum numbers. Fig. 9 shows three results obtained for the pyrrole $2v_{14}$ band, for values of δ ranging from 1.1 to 3.5. It is clear from these calculations that the unscaled anharmonic couplings are approximately a factor 2.4 too small to account for the off-resonant anharmonicity observed in the spectra. Calculations with $\delta = 1$ show very little fragmentation, and the transition occurs at too high a frequency. A very similar result was obtained for the triazine $v_6^1 + 2v_7^2$ initial state. The anharmonic shifts closest to experiment were obtained with scaling factors of 2.4 for both molecules, despite their different symmetries and the different initial states involved. These calculations also yielded effective numbers of states or dilution factors close to the experimental value.

There are two plausible sources for this discrepancy: the HF *ab-initio* surface could be too harmonic, or the spectral calculation does not take sufficiently many off-resonant couplings into account. Fig. 10 addresses the latter question. It shows the maximum contribution to the local number of coupled states^{27,50}

$$N_{loc} = \sum_i \mathcal{L}_{i0}^2 \quad [3.8]$$

made by a state in tier n to states in tier n-1. The first and second tiers show a significant decrease in the density of coupled states as the edge of the ΔE_{max} window is reached, indicating that most off-resonant states up to that point have been included. The third tier shows a high density up to the edge, indicating that second tier states near the edge are not yet coupled to all potentially important coupling partners. To test the effect of window truncation, a calculation with half the window size was also carried out. Although the dilution factor of the bright state decreased

somewhat, $\delta = 2.4$ was still needed to obtain the correct anharmonic shift and fragmentation. Therefore the truncation of off-resonant couplings results in computed dilution factors which are upper limits to the experimental values, but it cannot explain the higher anharmonicity required to reach the IVR threshold at $6,000 \text{ cm}^{-1}$.

This leaves the *ab-initio* surface as the likely culprit. Although the fits to eq. [3.3] are certainly not precise (average errors are on the order $\Delta E/E = 3$ and 5% for triazine and pyrrole), the diagonal and cross-anharmonic terms in eq. [3.3] follow the anharmonic contours of the ab initio potential points equally well at all energies up to $15,000 \text{ cm}^{-1}$, and do not appear more harmonic than the ab initio data at high energies. The most likely explanation is therefore that the HF surface itself overestimates the IVR threshold by underestimating the anharmonic coupling strength. This appears likely because HF wavefunctions overestimate dissociation energies, leading to a more harmonic surface at intermediate energies. The similarity of the two optimal scaling factors for pyrrole and triazine indicates that in these similar molecules, the anharmonicity is underestimated by very similar amounts.

The transition region for the onset of IVR is rather narrow as a function of δ . The IVR threshold is very sharply defined as a function of the anharmonic coupling strength. This is in accord with previous findings:^{20,27,61} the transition from a few off-resonant interactions to strong IVR occurs very rapidly as N_{loc} passes unity, and N_{loc} scales approximately as $\langle V \rangle^k$, where $\langle V \rangle$ is an average anharmonic coupling and k is the average length of coupling chains.⁵⁰ Evaluation of eq. [3.8] with the optimally scaled anharmonic potential constants yields $N_{loc} = 0.6$ for triazine and $N_{loc} = 1.8$ for pyrrole. The $2v_{14}$ band of pyrrole and the $v_6^1 + 2v_7^2$ of triazine indeed straddle the IVR threshold. In the following discussion we present all results with $\delta = 2.4$, which yields band origins close to the observed values.

4. Comparison of experimental and computed IVR dynamics

We now compare the first-principles IVR calculations (scaled by one non-hydrogenic anharmonicity parameter) with the low J experimental spectra. Table 4.1 lists the relevant

parameters of the measured and computed spectra, and figures 11 abd 12 compare the spectra for pyrrole and triazine.

The computed $2v_{14}$ IVR spectrum of pyrrole agrees qualitatively with the low resolution FTIR survey by Herman and coworkers. In particular, the calculation predicts a secondary feature to the blue of the main band, at about 6170 cm^{-1} . It turns out that this feature cannot be assigned to a simple normal mode state. As shown in figure 10 (left), there is a large number of first tier states which can contribute in the frequency range of interest. The eigenstate positions in the main IVR feature do not match exactly with the high resolution spectrum, but the widths of the features are comparable. Experimentally, we find a FWHM 0.13 cm^{-1} band, while the calculated band has a FWHM of 0.37 cm^{-1} , with weaker outliers up to $\pm 1\text{ cm}^{-1}$. In the region of interest, the density of states after diagonalization is near $15\text{-}20/\text{cm}^{-1}$. This is much lower than the experimentally observed value of $92\text{ states}/\text{cm}^{-1}$, and limited by the basis set size and number of tiers. However, the fraction of lines observed with an intensity $> 1/100$ that of the largest peak is $12/15$, nearly all lines, and in good agreement with the experimental finding that mixing in pyrrole is sufficiently extensive to light up all vibrational eigenstates near the IVR feature. Hence we are confident that the missing states would appear in the calculation, if we extended the basis set another tier and to the full density of states.

.The number of observed states ($> 1/100$ of the largest peak intensity) is about 20 in both experiment and calculation, so the dilution factors (or N_{eff}) are in even better agreement than the feature widths (table 4.1). Therefore the model correctly represents the amount of mixing and fragmentation, but does not fully capture the 'sharpness' of the IVR process. Why is the IVR feature so narrow despite average coupling matrix elements of 10s of cm^{-1} , and why does the calculation overestimate the width? These two questions are closely connected, and we consider this connection in more detail

For pyrrole at 6000 cm^{-1} , the IVR has highly off-resonant contributions due to coupling chains with more than two states. This is evident in fig. 10: the strongest couplings to the first tier come from a $\pm 200\text{ cm}^{-1}$ window around the bright state, but substantial couplings occur to off-resonant states more than 1000 cm^{-1} higher than the bright state. The exact nature of these couplings is of

course basis-dependent, but any feature basis will show qualitatively similar behavior.¹⁷ The narrow IVR feature is caused by a dominance of coupling *chains*, where the bright state couples to highly off-resonant gateways, which in turn couple back to states nearly isoenergetic with the bright state. Only nearly isoenergetic states receive intensity from state-mixing. We illustrate this indirect intensity transfer process by a simple three-state example. Consider the following Hamiltonian H with eigenvalues $\tilde{\epsilon}$ and eigenvector matrix M:

$$H = \begin{matrix} 0 & 0 & 10 \\ 0 & 0.1 & 11 \\ 10 & 11 & 1000 \end{matrix}, \quad \tilde{\epsilon} = \begin{matrix} -0.18 \\ 0.06 \\ 1000.2 \end{matrix}, \quad M = \begin{matrix} 0.816 & 0.507 & 0.010 \\ 0.578 & -0.866 & 0.011 \\ -0.014 & -0.003 & -0.999 \end{matrix} \quad [4.1]$$

The first basis state $|1\rangle$ corresponds to the bright state, and the second $|2\rangle$ to a nearly degenerate zero order state. They are not coupled directly, but only via a highly off-resonant gateway state $|3\rangle$, 1000 cm^{-1} higher in energy. The numbers shown are typical for what occurs in the full model. The first row of M shows that substantial intensity has been transferred from $|1\rangle$ to $|2\rangle$, leading to an IVR feature with eigenstates 0.24 cm^{-1} apart. The transferring state $|3\rangle$ remains dark. This mechanism only works when the zero order splitting between $|1\rangle$ and $|2\rangle$ is small compared to the effective coupling constant. For instance, if $E_2^{(0)}=10$ were substituted for 0.1 in H, no intensity transfer would occur. The effect is further exacerbated when higher coupling chains are involved.

The 2_{14} state of pyrrole lies just above the IVR threshold. The probability of having resonant gateway states is therefore very slow, and IVR is mediated by off-resonant coupling chains. These result in narrow features. The truncation effects of the basis set in fig. 10 somewhat reduce the contribution of longer coupling chains, and this results in a larger calculated width of the IVR feature in the spectrum.

Good agreement between experiment and calculation is also obtained for the pyrrole IVR feature. Due to the more complete basis, the effective number of states, dilution factor, and number of observed lines in the IVR feature are in near-quantitative agreement with experiment. Only the width of the IVR feature is again overestimated. This is because the more complete basis set in the energy window nonetheless does not alleviate the truncation problem which affects the off-resonant coupling chains. The good agreement of N_{eff} for the larger basis supports the contention made

above that the missing states in the calculated pyrrole spectrum are mostly due to basis incompleteness. Even as they stand, the present calculations have come closer to the eigenstate level of resolution than any previous work on molecules greater than tetratomics.

The tier structure used to generate the Hamiltonian is able to identify the gateway states postulated in section 2.3. Based on the number of substructures in the low J spectrum of figure 5, we expect to find roughly five gateway states. Generating a Hamiltonian up to a single tier and using the criterion $\mathcal{L}_{0i} > 0.1$ give rise to a total of four strongly coupled gateway states in pyrrole. Although the 0.1 cutoff is somewhat arbitrary, \mathcal{L}_{0i} should clearly be near unity for a bona fide gateway state. One can now identify the direction of energy flow in these anharmonic basis functions. Perhaps surprisingly, the strongest couplings from the bright states of pyrrole and triazine are not to other C-H stretches, but rather to states which contain a mixture of several in-plane ring deformation modes. In addition, out-of-plane C-H wagging modes are also mixed in quite early. This is not the first time this has been observed in the literature[Callegari, 2000 #832], but it serves to remind us that reduced dimensionality models in real space (e.g. "in-plane") can be inaccurate, even though the energy flow in state space is on a reduced dimensionality surface.

The ring deformation and wagging modes which contribute to IVR early on tend to move the same atoms as the bright state mode. This is due to the local coupling structure of the Hamiltonian.⁵¹ Energy degeneracy alone (as between two CH stretches) is not sufficient to induce mixing because couplings between localized modes decrease exponentially with the number of intervening bonds. This is most easily seen if we think of delocalized vibrations as arising from a tunneling between localized modes. The smallest molecular asymmetry (corresponding to unsymmetric wells in the tunneling analogy) is sufficient to localize the modes, particularly if the resulting local modes are separated by many bonds (corresponding to a broad barrier in the tunneling analogy).⁵⁰

The initial state in pyrrole is an overtone and lies at the edge of the state space in figure 1. The initial state of triazine is a combination band and therefore is more interior (actually, a 'surface state). Given the similar molecular structure and size of triazine and pyrrole, the more interior initial state of triazone (combination band) and the edge initial state of pyrrole sheds light on the

competing effects which control IVR in edge and interior states: interior states have more coupling partners (enhancing IVR), but smaller quantum numbers (decreasing the coupling matrix elements and restricting IVR). In the present case, the latter wins out and triazine $v_6^1 + 2v_7^2$ has a smaller N_{loc} than pyrrole 2¹⁴. However, because of its interior nature, the pyrrole initial state is more strongly coupled to first tier states involving out-of-plane modes (13 gateways). The more limited IVR in triazine proceeds out of plane even more rapidly than in pyrrole.

Considering the record size of the Hamiltonians in question and the extreme sensitivity of the spectral features, the calculations overall agree well with the experimental results. The improvements which would be required to achieve full quantitative agreement are: first, a potential surface which provides a very accurate description of the anharmonicity, and secondly, the inclusion of more off-resonant coupling effects, to reproduce the very narrow width of IVR features near threshold.

Acknowledgements

This work was supported by grants from the National Science Foundation (CHE-9986670 for MG and CHE-\ for KL and GS). MG was a Dreyfus Teacher-Scholar while this work was carried out, and AC was supported by the Swiss National Science Foundation.

Table 2.1 Parameters for the simulation of the molecular beam spectra of pyrrole and triazine

	Ground state (Ref. ²⁹)	Upper state (Ref. ³³)	Ground state (Ref. ³⁴)	Upper state (from fit)
	Pyrrole		Triazine	
<i>T</i>		6 K		4 K
ν_0 /cm ⁻¹		6145.7		5981.27
A /cm ⁻¹	0.30456	0.3022	0.30456	0.3022
B /cm ⁻¹	0.30025	0.3011	0.30025	0.3011
C /cm ⁻¹	0.15117	0.1590	0.15117	0.1590

Table 2.2 Statistical properties of pyrrole spectrum for various IVR multiplets. Number of observed (N_d) and effective (N_{eff}) coupled states. Density of observed states () and average coupling to the bright state V_{rms} . See text for details.

$J'_{K'aK'c}$	$J'_{K'aK'c}$	N_d	N_{eff}	/states/cm $^{-1}$	V_{rms}	GR
				/10 $^{-2}$ cm $^{-1}$		/ps
2 ₀₂	1 ₀₁ (3 ₀₃)	20	15.1 (12.4)	92	1.24 (1.21)	60 (63)
3 ₀₃	2 ₀₂ (4 ₀₄)	21	15.7 (12.6)	112	0.926 (0.892)	88 (95)
4 ₀₄	3 ₀₃ (5 ₀₅)	32	17.6 (18.2)	166	0.682 (0.725)	109 (98)
5 ₀₅	4 ₀₄ (6 ₀₆)	23	16.6 (18.0)	154	0.712 (0.715)	108 (107)
6 ₀₆	5 ₀₅ (7 ₀₇)	19	15.4 (13.7)	243	0.595 (0.606)	98 (95)
7 ₀₇	6 ₀₆ (8 ₀₈)	23	19.9 (19.2)	251	0.595 (0.603)	95 (92)
8 ₀₈	7 ₀₇ (9 ₀₉)	18	15.7 (15.8)	216	0.615 (0.647)	103 (93)
2 ₂₁	2 ₂₀ (3 ₂₂)	27	18.6 (15.1)	147	0.934 (0.901)	66 (71)
3 ₁₂	2 ₁₁ (4 ₁₃)	22	13.1 (14.4)	110	0.808 (0.722)	117 (147)
4 ₂₃	3 ₂₂ (5 ₂₄)	25		145	0.584 (0.698)	170 (119)

Table 2.3 Parameters used in the level spacing analysis of pyrrole. See text for details.

$J'_{K^*aK^*c}$	f	app	
2_{02}	< 0.1	90	> 900
3_{03}	< 0.16	130	> 810
4_{04}	< 0.18	180	> 1000
5_{05}	< 0.3	165	> 550
6_{06}	< 0.3	240	> 720
7_{07}	< 0.3	265	> 590
8_{08}	< 0.4	210	> 525

Table 2.4 Statistical properties of triazine spectrum for various IVR multiplets. Number of observed (N_d) and effective (N_{eff}) coupled states, and density of observed states (). See text for details.

			$J=0$	$J=1$	$J=2$	$J=3$	$J=4$
$K=1$	0	/ps	115	115	125	90	145
		/states/cm ⁻¹	90	60	68	94	142
	N_d		7	6	6	7	10
	N_{eff}		3.5	3.8	3.7	3.7	4.2
$K=0$	1	/ps		90	80	100	
		/states/cm ⁻¹		80	73	40	
	N_d			5	4	3	
	N_{eff}			3.2	2.2	1.5	
$K=1$	2	/ps			230	175	120
		/states/cm ⁻¹			65	110	58
	N_d				4	7	6
	N_{eff}				1.5	3.1	2.6

Table 3.1 HF 6-31G** Equilibrium geometries for Pyrrole and triazine. Atom numbers from figure 8 are added where identification of a coordinate would be ambiguous.

Pyrrole	Triazine
$r_{CN}^{eq} = 1.363 \text{ \AA}$	$r_{CN}^{eq} = 1.318 \text{ \AA}$
$r_{C2C3}^{eq} = 1.358 \text{ \AA}$	$r_{CH}^{eq} = 1.076 \text{ \AA}$
$r_{NH}^{eq} = 0.991 \text{ \AA}$	$\alpha_{NCN}^{eq} = 125.5^\circ$
$r_{CH7}^{eq} = 1.070 \text{ \AA}$	$\alpha_{CNC}^{eq} = 114.4^\circ$
$r_{CH8}^{eq} = 1.070 \text{ \AA}$	$\beta_{ijk}^{eq} = 117.2^\circ$
$\beta_{C2N1H6}^{eq} - \beta_{C5N1H6}^{eq} = 0.0^\circ$	$\gamma_{ijkl}^{eq} = \tau_{ijkl}^{eq} = 0^\circ$
$\beta_{N1C2H7}^{eq} - \beta_{C3C2H7}^{eq} = 9.4^\circ$	
$\beta_{C2C3H8}^{eq} - \beta_{C4C3H8}^{eq} = 1.0^\circ$	
$\alpha_{CNC}^{eq} = 109.5^\circ$	
$\alpha_{NCC}^{eq} = 108.2^\circ$	
$\gamma_{ijkl}^{eq} = \tau_{ijkl}^{eq} = 0^\circ$	

Table 3.2 Valence coordinates, displacement coordinates, and fitted parameters of the f coordinates for the potential surface of triazine. See figure 8 for atom numbering. All m_i of eq. [3.5] were held fixed at 6 (Lennard Jones form). The parameters shown do no include the scaling factors α_i or δ_i described in section 3. Analogous parameters for pyrrole are given in ref. ⁵³.

$s_1 = r_{C_1N_2}$				
$s_2 = r_{N_2C_3}$	$x_i = \frac{(s_i - r_{CN}^{eq})}{r_{CN}^{eq}}$			
$s_3 = r_{C_3N_4}$		$d_i = 160$	$\alpha_i = 3.849 \pm 0.002$	$b_i = 1$
$s_4 = r_{N_4C_5}$	$i = 1 - 6$			
$s_5 = r_{C_5N_6}$				
$s_6 = r_{C_1N_6}$				
$s_7 = r_{C_1H_9}$	$x_i = \frac{(s_i - r_{CH}^{eq})}{r_{CH}^{eq}}$			
$s_8 = r_{C_3H_8}$		$d_i = 200$	$\alpha_i = 2.113 \pm 0.001$	$b_i = 1$
$s_9 = r_{C_5H_7}$	$i = 7 - 9$			
$s_{10} = N_6C_1N_2$	$x_i = s_i - \alpha_{NCN}^{eq}$			
$s_{11} = N_2C_3N_4$	$i = 10 - 12$	$d_i = 190$	$\alpha_i = 1.492 \pm 0.002$	$b_i = 1/2$
$s_{12} = N_4C_5N_6$				
$s_{13} = N_2C_1H_9$				
- $N_6C_1H_9$	$x_i = s_i$			
$s_{14} = N_4C_3H_8$	$i = 13 - 15$	$d_i = 190$	$\alpha_i = 0.506 \pm 0.001$	$b_i = 1/2$
- $N_2C_3H_8$				
$s_{15} = N_6C_5H_7$				
- $N_4C_5H_7$				
$s_{16} = N_2C_1N_6H_9$	$x_i = s_i$			
$s_{17} = N_4C_3N_2H_8$	$i = 16 - 18$	$d_i = 190$	$\alpha_i = 0.824 \pm 0.001$	$b_i = 1/2$
$s_{18} = N_6C_5N_4H_7$				
$s_{19} = N_6C_1N_2C_3$	$x_i = s_i$			
$s_{20} = N_2C_3N_4C_5$	$i = 19 - 21$	$d_i = 190$	$\alpha_i = 0.605 \pm 0.002$	$b_i = 1/2$
$s_{21} = N_4C_5N_6C_1$				

Table 3.3 – Potential constants for triazine in eq. [3.4]. Analogous parameters for pyrrole are given in ref. ⁵³.

$F_{CNCN}^{(1)} = 0.271 \pm 0.001$	$F_{CHCH}^{(1)} = 0.003 \pm 0.000$	$F_{\alpha\alpha}^{(1)} = 0.062 \pm 0.003$
$F_{CNCN}^{(2)} = 0.185 \pm 0.001$	$F_{CH\alpha}^{(1)} = -0.060 \pm 0.002$	$F_{\alpha\beta}^{(1)} = 0.001 \pm 0.002$
$F_{CNCN}^{(3)} = 0.216 \pm 0.002$	$F_{CH\alpha}^{(2)} = -0.009 \pm 0.001$	$F_{\alpha\beta}^{(2)} = 0.089 \pm 0.002$
$F_{CNCH}^{(1)} = 0.045 \pm 0.001$	$F_{CH\beta}^{(1)} = 0.000 \pm 0.001$	$F_{\beta\beta}^{(1)} = -0.041 \pm 0.001$
$F_{CNCH}^{(2)} = -0.012 \pm 0.001$	$F_{CH\beta}^{(2)} = -0.007 \pm 0.001$	$F_{\gamma\gamma}^{(1)} = -0.065 \pm 0.003$
$F_{CNCH}^{(3)} = -0.001 \pm 0.001$		$F_{\gamma\pi}^{(1)} = 0.871 \pm 0.004$
		$F_{\gamma\pi}^{(2)} = -0.093 \pm 0.006$
		$F_{\gamma\pi}^{(3)} = 0.348 \pm 0.005$
		$F_{\tau\tau}^{(1)} = 0.202 \pm 0.008$

Table 3.4 Estimated experimental and calculated normal mode harmonic frequencies for triazine. The frequencies shown here are from the unscaled potential surface in tables 3.2 and 3.3. For IVR simulations, scaling factors $i = (\omega_{\text{exp}} / \omega_{\text{calc}})^{1/2}$ were used for all modes to bring the harmonic frequencies into agreement with experiment.

Symmetry	Mode	Experimental	Calculated
A_1'	1	3042	3319
	2	1124	1201
	3	992	1078
A_2'	4	(1375)	1518
	5	(1000)	1138
E'	6	3056	3308
	7	1554	1723
	8	1410	1585
	9	1167	1259
	10	678	690
A_2''	11	925	1051
	12	737	805
E''	13	1034	1140
	14	339	429

Table 3.5 Estimated experimental and calculated normal mode harmonic frequencies for pyrrole. The frequencies shown here are from the unscaled potential surface in tables 3.2 and 3.4. For IVR simulations, scaling factors $i = (\text{exp}/\text{calc})^{1/2}$ were used for all modes to bring the harmonic frequencies into exact agreement.

Symmetry	Mode	Estd. experimental cm ⁻¹	Unscaled calculated cm ⁻¹
A ₁	1	3527	3943
	2	3148	3439
	3	3125	3413
	4	1470	1638
	5	1391	1541
	6	1148	1256
	7	1074	1167
	8	1018	1107
	9	880	959
B ₁	10	3140	3446
	11	3116	3387
	12	1548	1730
	13	1424	1597
	14	1287	1426
	15	1134	1245
	16	1049	1156
	17	863	941
	18	(866)	995
A ₂	19	(712)	796
	20	(615)	674
	21	826	976
	22	720	833
B ₂	23	626	663
	24	474	475

Table 4.1. Comparison of experimental spectral data with the calculations. The calculations were for $J = 0$; for pyrrole, the lowest $J = 2$ $K_a = 0$ rotational subband is listed, and for triazine the ${}^P P_1(1)$ rotational subband.

	Pyrrole		Triazine	
	Experimental	Calculation	Experimental	Calculation
FWHM (cm^{-1})	0.13	0.37	0.05	0.15
$N_{\text{obs}} (1/\text{cm}^{-1})^{\dagger 1}$	92 (93)	12/15	90 (63)	15/41
$N_d^{\dagger 2}$	20	23	7	6
N_{eff}	15.1	7.7	3.5	2.9
N_{loc}	-	1.8	-	0.6
	0.07	0.15	0.29	0.35
$\tau_{\text{GR}} (\text{ps})$	60	20	115	40

^{†1} In parenthesis: harmonic Laplace transform value. Calculation: from 2 cm^{-1} interval around main bright state feature, out of the maximum expected based on the vibrational basis set density.

^{†2} Experiment: total number of eigenstates detected correlating to the bright state at a signal-to-noise ratio of approx. 100; calculation: total number of states at least 1/100 the intensity of the strongest state in a $\pm 1 \text{ cm}^{-1}$ window around center of feature.

Figure Captions

1. Relation between state space and vibrational spectrum, illustrating some of the quantities used in the paper to characterize IVR. Top row: 3 coordinates from the $3N-6$ dimensional state space; open circles are zero order states; vertices indicate significant couplings. N_{loc} is the local number of coupled states. Bottom row: resulting fragmented spectra. N_{eff} is the effective number of states in the spectrum, and γ is the dilution factor as defined in eq. [1.1]; the number of vibrational states observed in an IVR feature state, N_{obs} , depends on the signal-to-noise ratio. Left column: coupling strength a below the IVR threshold; only isolated resonances occur in the spectrum. Right column: $N_{\text{loc}} > 1$ allows anisotropic flow of the IVR wave packet in state space, resulting in a feature state with width γ_{IVR}^{-1} .
2. (Top) Single-resonance high resolution infrared spectrum of the 2_{14} band of pyrrole. (Bottom) Effective-Hamiltonian simulation of the above spectrum.
3. (Top) Single-resonance high resolution infrared spectrum of the $6^+ 2_7^2$ band of triazine. (Bottom) Effective-Hamiltonian simulation of the above spectrum.
4. Comparison of single-resonance and double-resonance measurements for pyrrole.
5. Stick-spectrum of the assigned rotational transitions of the 2_{14} band of pyrrole. Each stick corresponds to a different vibrational eigenstate. Frequencies are plotted as a difference from the band origin. As rotational energy increases features become narrower and less clumpy, indicating the onset of Coriolis coupling.
6. Low-resolution spectrum of the overtone region of triazine. Several vibrational bands are present. They are expected to mix significantly, making any identification of the bright state nominal. The largest such band at 5980 cm^{-1} was chosen for our investigations, tentatively assigned to the $6^+ 2_7^2$ band.
7. Representative high-resolution data from the $6^+ 2_7^2$ band of triazine. The + indicates a state identified to be in the ${}^P\text{P}_1(1)$ transition manifold. Other transitions have been reliably assigned to the Q-branch.

8. Pictorial definition of the curvilinear coordinates used in the full-dimensional quantum calculations. Top: Numbering of the atoms for pyrrole and triazine. Bottom: definition of stretch and bend coordinates, and auxiliary vectors used to calculate wag and torsion coordinates. The wagging coordinate is the cosine of the angle between $\vec{r}_{12} \times \vec{r}_{13}$ and \vec{r}_{14} . The torsional coordinate is the angle between $\vec{r}_{12} \times \vec{r}_{13}$ and $\vec{r}_{31} \times \vec{r}_{34}$.
9. Two-tier pyrrole calculations as a function of the anharmonic correction factor δ . The bottom axis is the energy offset from the observed band origin. As δ increases, fragmentation increases, and the energy red-shifts toward the observed band origin. The amount of fragmentation is a rather sharply varying function of δ . For both pyrrole and triazine, increasing δ to place the band origin near the experimental value also introduces the correct amount of fragmentation and IVR linewidth. This indicates that insufficient anharmonicity of the fitted SCF force field is mainly responsible for overestimating the IVR threshold energy.
10. Directly coupled local density of states for the pyrrole calculation, as a histogram of N_{loc} as a function of energy difference from the band origin. Left: most of the states which are directly coupled to the bright state are clumped close in energy (within 200 cm^{-1}) of the bright state, but significant off-resonant contributions exist up to 1500 cm^{-1} . Middle: for the second tier, this distribution is already much wider. Right: in the third tier, the distribution is so wide that energy window truncation precludes the meaningful use of further tiers.
11. A comparison of the low-resolution, experimental high-resolution, and calculated spectra of the 2_{14} band of pyrrole. Top: a low resolution FTIR spectrum from Herman, et al. /ref. Left middle: a stick-spectrum of the assigned bands in the single-resonance spectrum. Right middle: an composite low resolution view of the calculated ($J=0$) vibrational spectrum combining a small window (higher resolution) and large window calculation. The weak band above the main peak of the experimental low resolution spectrum is also revealed by the calculation. Bottom left: an expanded stick spectrum of the $2_{02} - 1_{01}$ band. Bottom right: the calculated ($J=0$) feature. With anharmonic rescaling 2.4, the linewidth and band origin are in good agreement with the experimental data. The dilution factor (table 4.1) is slightly too

large, probably because the incomplete basis set misses a few eigenstates within the IVR feature.

- 12 Left: A stick spectrum of the $J=0 \rightarrow 1$ band of triazine. Right: The calculated ($J=0$) band, which has a very similar dilution factor, but somewhat overestimates the dephasing rate, as discussed in the text.

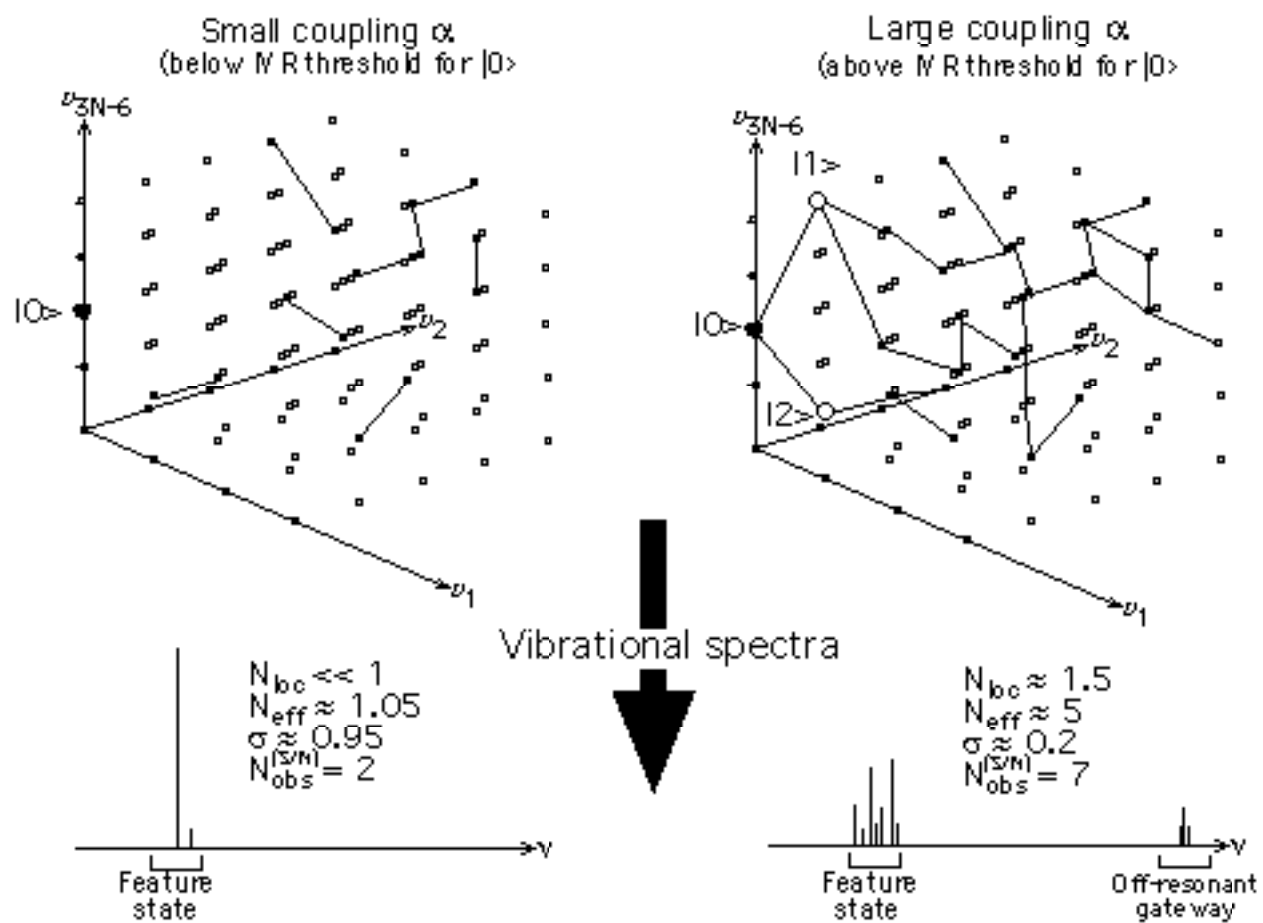
References

- ¹ S. Schofield and P. G. Wolynes, *J. Chem. Phys.* **98**, 1123 (1993).
- ² M. Gruebele and R. Bigwood, *Int. Rev. Phys. Chem.* **17**, 91 (1998).
- ³ A. A. Stuchebrukhov and R. A. Marcus, *J. Chem. Phys.* **98** (8), 6044 (1993).
- ⁴ R. J. Minehardt, J. D. Adcock, and R. E. Wyatt, (1998).
- ⁵ R. Bigwood, B. Milam, and M. Gruebele, *Chem. Phys. Lett.* **287**, 333 (1998).
- ⁶ A. Viel and C. Leforestier, *J. Chem. Phys.* **in press** (2000).
- ⁷ J. E. Gambogi, J. H. Timmermans, K. K. Lehmann, and G. Scoles, *J. Chem. Phys.* **99** (11), 9314 (1993).
- ⁸ K. K. Lehmann, G. Scoles, and B. H. Pate, *Annu. Rev. Phys. Chem.* **45**, 241 (1994).
- ⁹ A. Callegari, U. Merker, P. Engels, H. K. Srivastava, K. K. Lehmann, and G. Scoles, *J. Chem. Phys.* (2000).
- ¹⁰ B. H. Pate, *J. Chem. Phys.* **110**, 1990 (1999).
- ¹¹ O. V. Boyarkin, T. R. Rizzo, and D. S. Perry, *J. Chem. Phys.* **110** (23), 11346 (1999); M. Silva, R. Jongma, R. W. Field, and A. M. Wodtke, *Ann. Rev. Phys. Chem.* (2001).
- ¹² M. Hippler and M. Quack, *Ber. Bunsenges. Phys. Chem.* **101** (3), 356 (1997); J. E. Gambogi, R. P. L'Esperance, K. K. Lehmann, B. H. Pate, and G. Scoles, *J. Chem. Phys.* **98**, 1116 (1993).
- ¹³ P. G. Smith and J. D. McDonald, *J. Chem. Phys.* **96** (10), 7344 (1992).
- ¹⁴ M. Gruebele, *Proc. Nat. Acad. Sci. USA* **95**, 5965 (1998).
- ¹⁵ M. P. Jacobson, J. P. O'Brien, R. J. Silbey, and R. W. Field, *J. Chem. Phys.* **109**, 121 (1999).
- ¹⁶ D. M. Leitner and P. G. Wolynes, *J. Phys. Chem. A* **101** (4), 541 (1997).

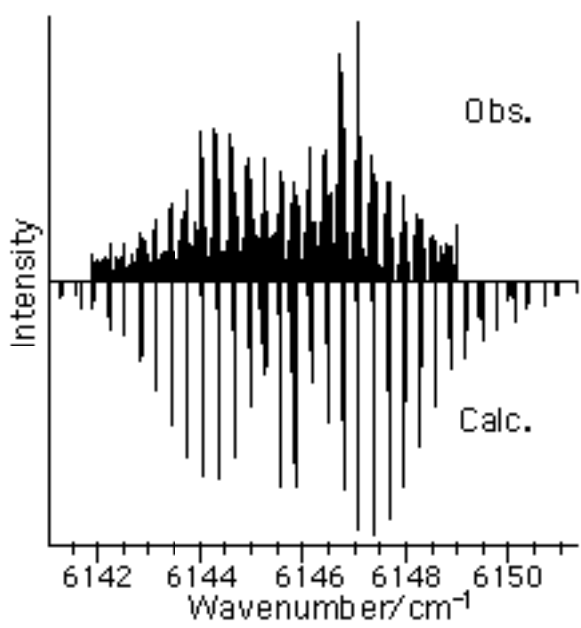
- ¹⁷ V. Wong and M. Gruebele, *J. Phys. Chem.* **103**, 10083 (1999).
- ¹⁸ M. Gruebele, *Adv. Chem. Phys.* **114**, 193 (2000).
- ¹⁹ R. A. Marcus, *J. Chem. Phys.* **20** (1), 359 (1952).
- ²⁰ A. A. Stuchebrukhov, M. V. Kuzmin, V. N. Bagratashvili, and V. S. Lethokov, *Chem. Phys.* **107**, 429 (1986).
- ²¹ D. E. Logan and P. G. Wolynes, *Phys. Rev. B* **36** (8), 4135 (1987).
- ²² S. H. Courtney, M. W. Balk, L. A. Philips, and G. R. Fleming, *J. Chem. Phys.* **89**, 6697 (1988); D. M. Leitner and P. G. Wolynes, *Chem. Phys. Lett.* **280**, 411 (1997).
- ²³ M. Quack, *Faraday Discuss. Chem. Soc.* **75**, 359 (1983).
- ²⁴ A. A. Stuchebrukhov, A. Mehta, and R. A. Marcus, *J. Phys. Chem.* **97**, 12491 (1993).
- ²⁵ S. A. Schofield and P. G. Wolynes, *J. Phys. Chem.* **99**, 2753 (1995).
- ²⁶ J. Go, T. J. Cronin, and D. S. Perry, *Chem. Phys.* **175**, 127 (1993).
- ²⁷ R. Bigwood, M. Gruebele, D. M. Leitner, and P. G. Wolynes, *Proc. Natl. Acad. Sci. USA* **95**, 5960 (1998).
- ²⁸ R. C. Lord and F. A. Miller, *J. Chem. Phys.* **10**, 328 (1942).
- ²⁹ G. Wlodarczak, L. Martinache, J. Demmaison, and B. P. Van Eijck, *J. Mol. Spectr.* **127**, 200 (1988).
- ³⁰ T. D. Klots, R. D. Chirico, and W. V. Steele, *Spectrochimica Acta* **50**, 765 (1994); C. Douketis and J. P. Reilly, *J. Chem. Phys.* **96**, 3431 (1992); A. Mellouki, R. Georges, M. Herman, D. L. Snavely, and S. Leytner, *Chem. Phys.* **220**, 311 (1997).
- ³¹ A. Held and M. Herman, *Chem. Phys.* **190**, 407 (1995).
- ³² Y. Xie, K. Fan, and J. E. Boggs, *Mol. Phys.* **58**, 401 (1986).

- ³³ L. Lubich and S. Oss, J. Chem. Phys. **106**, 5379 (1997).
- ³⁴ C. A. Morrison, B. A. Smart, D. W. H. Rankin, H. E. Robertson, M. Pfeffer, W. Bodenmüller, R. Ruber, B. Macht, A. Ruoff, and V. Typke, J. Phys. Chem. A **101** (10029-10038) (1997).
- ³⁵ A. Navarro, J. J. L. Gonzales, M. F. Gomez, F. Marquez, and J. C. Otero.
- ³⁶ G. Fisher, A. U. Nwankwoala, M. P. Ollif, and A. P. Scott, J. Mol. Spectr. **161**, 388 (1993).
- ³⁷ W. Bodenmüller, A. Ruoff, and L. Manceron, Z. Naturforsch. **47A**, 1197 (1992).
- ³⁸ W. Pyckhout, I. Callaerts, C. van Alsenoy, and H. J. Geise, J. Mol. Struct. **147**, 321 (1986).
- ³⁹ A. Navarro, J. J. L. Gonzales, G. J. Kearley, J. Tomkinson, S. F. Parker, and D. S. Sivia, Chem. Phys. **200**, 395 (1995).
- ⁴⁰ S. Creuzet and J. Langlet, Chem. Phys. Lett. **208**, 511 (1993).
- ⁴¹ T. Gejo, J. A. Harrison, and J. R. Huber, J. Phys. Chem. **100**, 13941 (1996).
- ⁴² G. Herzberg, *Molecular Spectra and Molecular Structure, Vol. II. Infrared and Raman Spectra of Polyatomic Molecules*. (Van Nostrand, New York, 1945).
- ⁴³ K. K. Lehmann, J. Phys. Chem. **95**, 7556 (1991).
- ⁴⁴ D. Romanini and K. K. Lehmann, J. Chem. Phys. **98** (8), 6437 (1993).
- ⁴⁵ T. A. Brody, J. Flores, J. B. French, P. A. Mello, A. Pandey, and S. S. M. Wong, Rev. Mod. Phys. **53** (3), 385 (1981).
- ⁴⁶ A. McNichols and J. T. Carrington, Chem. Phys. Lett. **202** (6), 464 (1993).
- ⁴⁷ W. J. Bullock, D. K. Adams, and W. D. Lawrence, J. Chem. Phys. **93**, 3085 (1990).
- ⁴⁸ R. Bigwood and M. Gruebele, Chem. Phys. Lett. **235**, 604 (1995).
- ⁴⁹ D. Madsen, R. Pearman, and M. Gruebele, J. Chem. Phys. **106** (14), 5874 (1997).

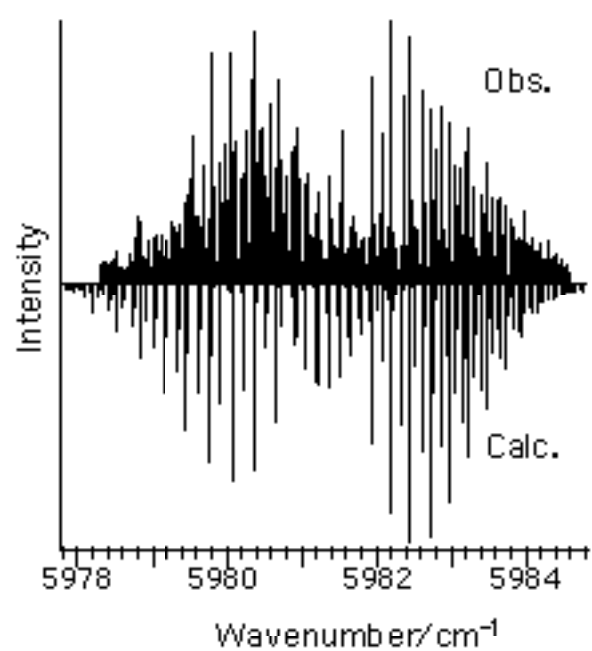
- ⁵⁰ R. Pearman and M. Gruebele, J. Chem. Phys. **108**, 6561 (1998).
- ⁵¹ R. Pearman and M. Gruebele, Z. Phys. Chemie **214** (11), 1439 (2000).
- ⁵² R. Bigwood and M. Gruebele, ACH Models in Chemistry **134** (1997).
- ⁵³ R. Pearman, Ph.D., University of Illinois, 2001.
- ⁵⁴ M. Gruebele, Mol. Phys. **69**, 475 (1990).
- ⁵⁵ B. Strickler and M. Gruebele, Chem. Phys. Lett. (2001).
- ⁵⁶ M. Gruebele, J. Phys. Chem. **100**, 12183 (1996); V. Wong and M. Gruebele, Phys. Rev. A **63**, 22502 (2001).
- ⁵⁷ M. Gruebele, J. Chem. Phys. **104** (6), 2453 (1996); M. Gruebele, J. Phys. Chem. **100**, 12178 (1996).
- ⁵⁸ S. W. Huang and T. Carrington, J. Chem. Phys. **112**, 8765 (2000).
- ⁵⁹ V. A. Mandelshtam and H. S. Taylor, J. Chem. Phys. **107**, 6756 (1997).
- ⁶⁰ M. Gruebele, Chem. Phys. (2001).
- ⁶¹ D. E. Logan and P. G. Wolynes, J. Chem. Phys. **93** (7), 4994 (1990).



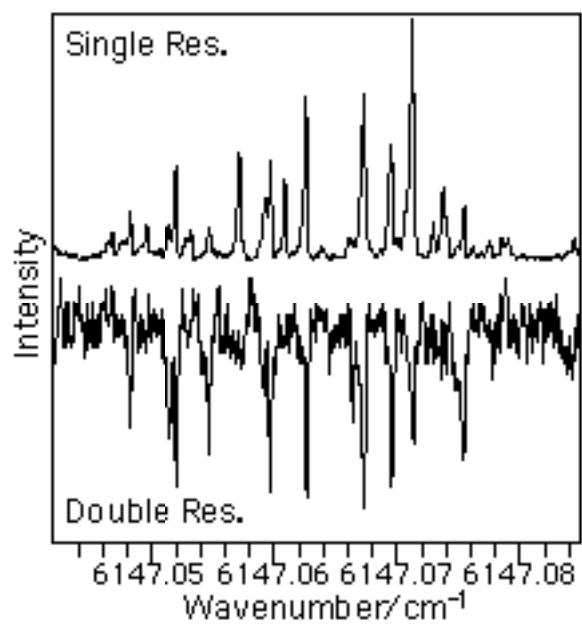
Callegari et al., Fig. 1



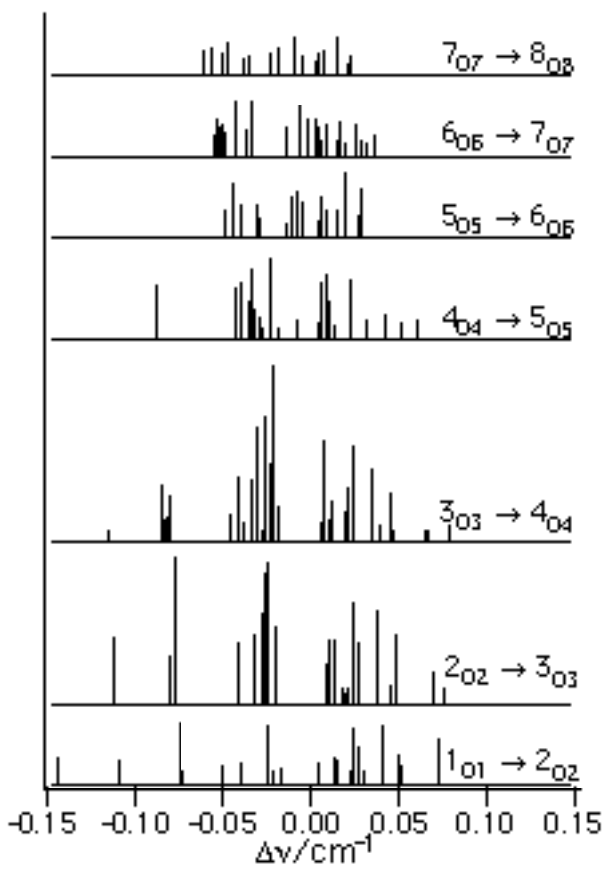
Callegari et al., Fig. 2



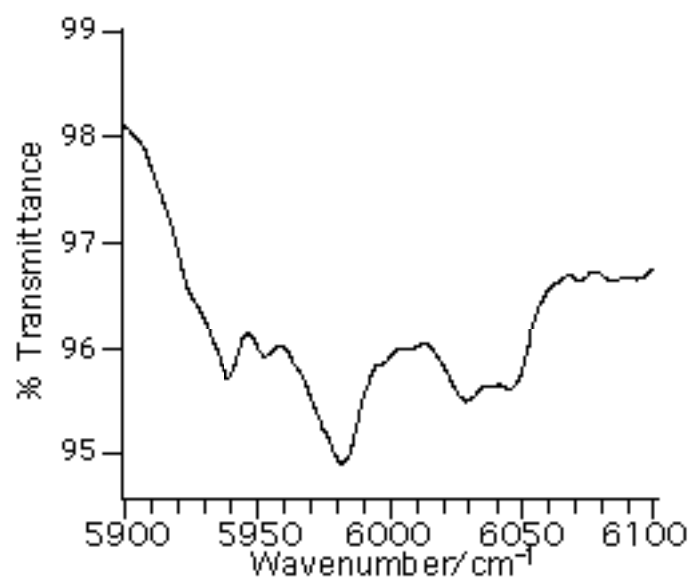
Callegari et al., Fig. 3



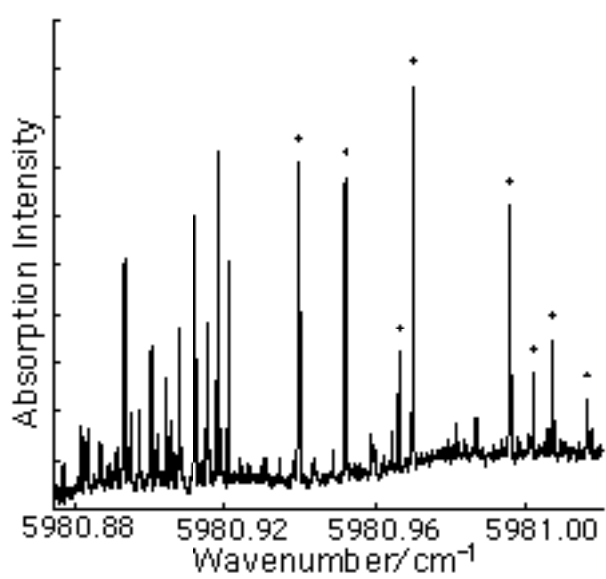
Callegari et al., Fig. 4



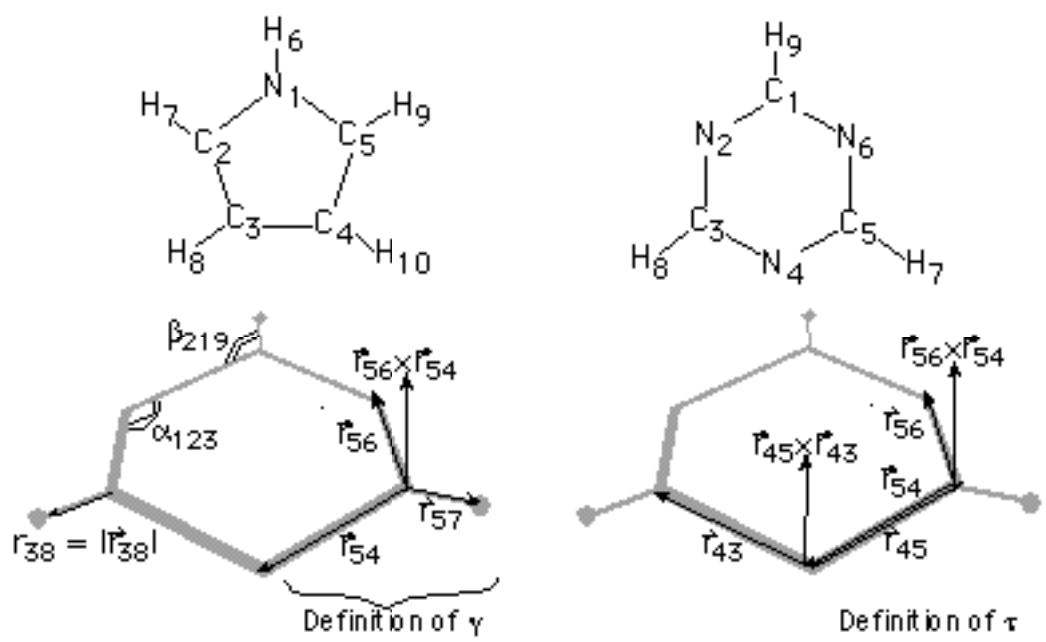
Callegari et al., Fig. 5



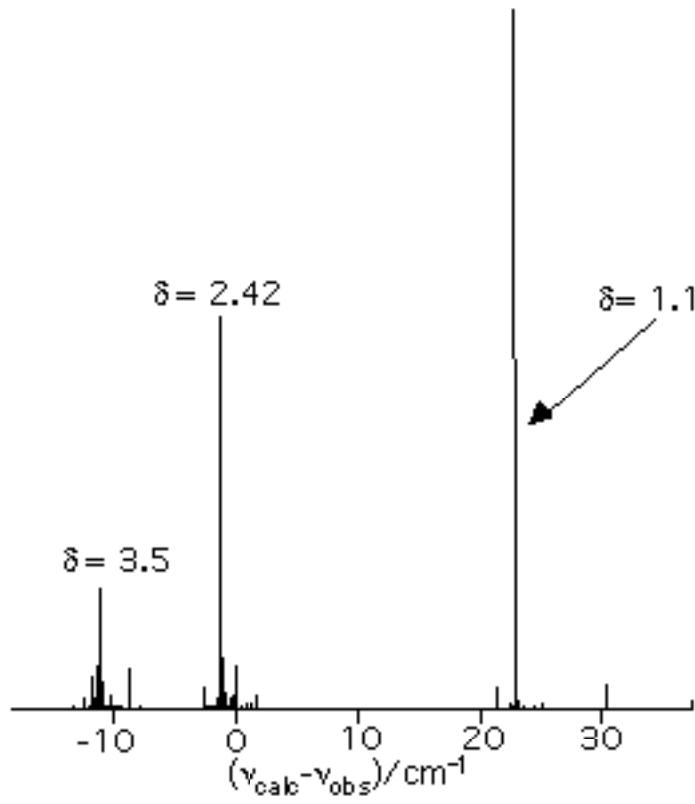
Callegari et al., Fig. 6



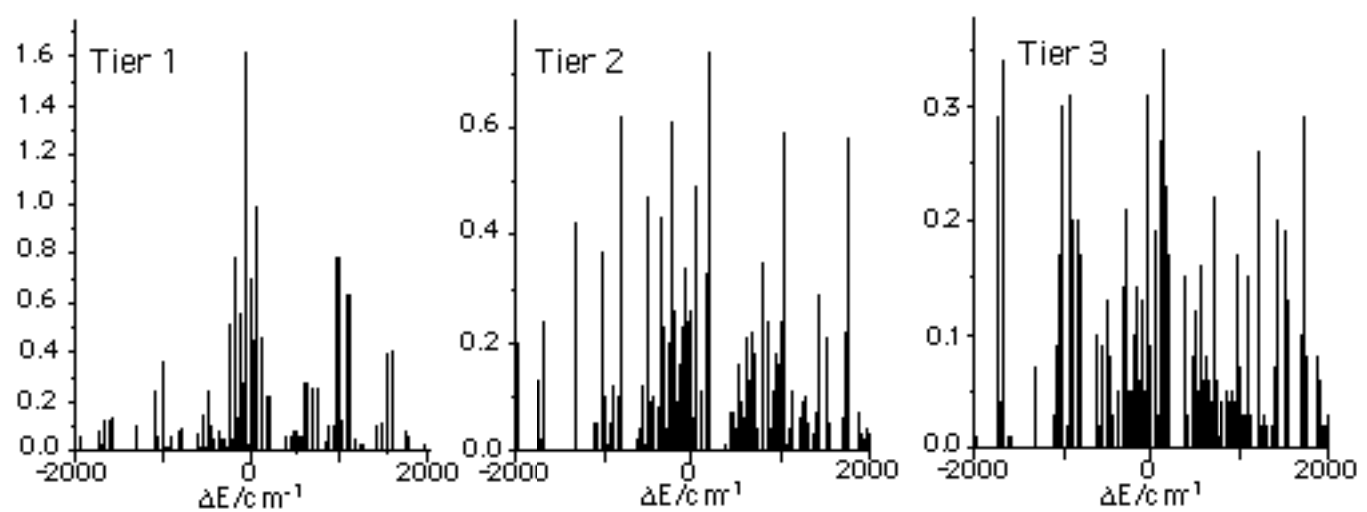
Callegari et al., Fig. 7



Callegari et al., Fig. 8

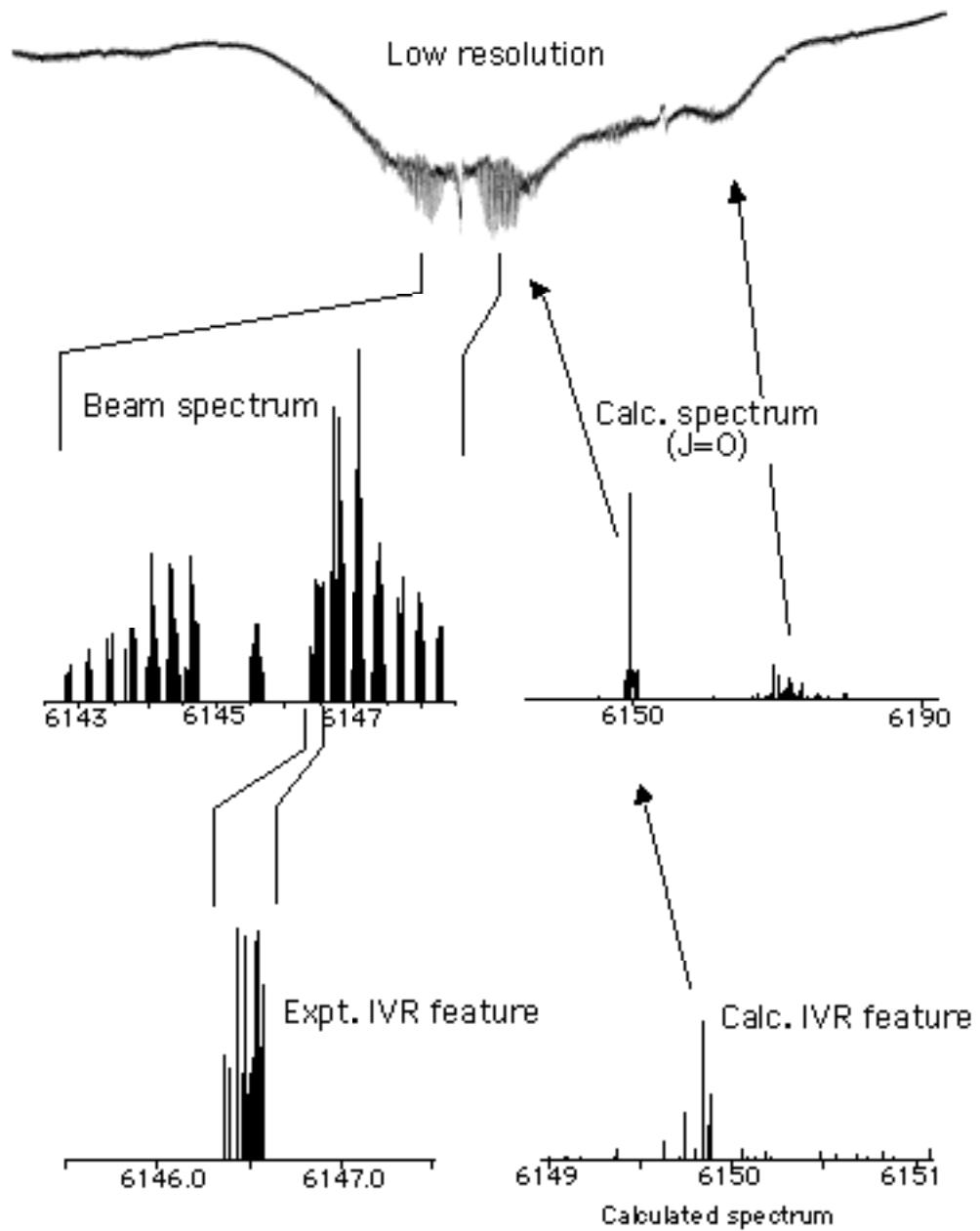


Callegari et al., Fig. 9

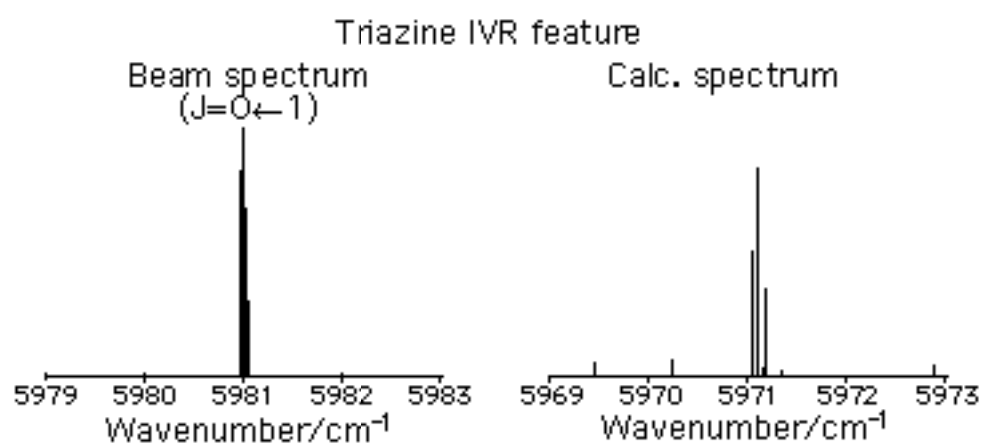


Callegari et al., Fig. 10

Experimental and calculated pyrrole spectra



Callegari et al., Fig. 11



Callegari et al., Fig. 12